RSC Advances

PAPER

View Article Online
View Journal | View Issue

Cite this: *RSC Adv.*, 2025, **15**, 5766

Newly predicted halide perovskites Mg_3AB_3 (A = N, Bi; B = F, Br, I) for next-generation photovoltaic applications: a first-principles study

Mayeen Uddin Khandaker, *[abc] Hamid Osman, [d] Shams A. M. Issa,[e] M. M. Uddin,*[f] Md. Habib Ullah,[g] Hajir Wahbi[h] and M. Y. Hanfi[ij]

The research examines the exceptional physical characteristics of Mg_3AB_3 (A = N, Bi; B = F, Br, I) perovskite compounds through density functional theory to assess their feasibility for photovoltaic applications. Mechanical characterization further supports their stability where out of all the compounds, Mg_3BiI_3 demonstrates high ductility, while Mg_3NF_3 and Mg_3BiBr_3 possess a brittle nature. The calculated elastic constants and anisotropy factors also substantiate their mechanical stability, while there is an observed declining trend in Debye temperature with increase in atomic number. From the electronic point of view, Mg_3NF_3 can be considered as a wide-bandgap insulator with the bandgap of 6.789 eV, whereas Mg_3BiBr_3 and Mg_3BiI_3 can be classified as semiconductors suitable for photovoltaic applications bandgaps of 1.626 eV and 0.867 eV, respectively. The optical characteristics of such materials are excellent and pronounced by high absorption coefficients, low reflectivity, and good dielectrics, which are very important in the collection of solar energy. Among them, Mg_3BiBr_3 and Mg_3BiI_3 possess high light absorption coefficient, moderate reflectivity, and good electrical conductivity, indicating that they are quite suitable for applying the photoelectric conversion materials for solar cells. In addition, thermal analysis shows that Mg_3NF_3 is a good heat sink material, Mg_3BiBr_3 and Mg_3BiI_3 are favorable for thermal barrier coating materials. Due to their high absorption coefficients, low reflectance and suitable conductivity, both Mg_3BiBr_3 and Mg_3BiI_3 could be regarded as the most appropriate materials for the creation of the next generation of photovoltaic converters.

Received 2nd January 2025
Accepted 14th February 2025

DOI: 10.1039/d4ra09093d

rsc.li/rsc-advances

1 Introduction

Photovoltaic (PV) technology plays a crucial role in reducing environmental pollution and decreasing reliance on fossil fuels, positioning it as a key solution for sustainable energy production.[1] Materials like silicon (Si), GaAs, CdTe, and Cu(In,Ga)(S,Se)$_2$ (CIGS) have achieved remarkable advancements in PV applications, with crystalline silicon dominating commercialization due to its high power conversion efficiency (PCE), stability, and radiation resistance.[2,3] However, the non-ideal, indirect bandgap of silicon and high fabrication costs limit further development.[4] Since 2009,[5] halide perovskites have emerged as transformative materials in solar energy, characterized by optimal bandgaps, high absorption coefficients, exceptional charge carrier mobility, and defect tolerance.[6,7] These features have driven their PCE from 3.8% to 25.5% within a decade.[8] However, challenges such as the toxicity and instability of lead-based perovskites hinder their scalability. Addressing these issues has led to intensive research into lead-free alternatives, though their efficiency and stability often lag behind traditional perovskites.[9,10]

Among lead-free candidates, the A_3MX_3 perovskite family, featuring elements like A = Mg^{2+}, Ba^{2+}, Sr^{2+}, Ca^{2+}, and M = Sb^{3-}, As^{3-}, P^{3-}, and halides (X = F^-, Cl^-, Br^-, I^-), has garnered attention. These compounds, with a cubic structure in the $Pm\bar{3}m$ space group, exhibit direct bandgaps, high stability, and strong optoelectronic properties, making them ideal for PV applications.[11–15] Notably, the Shockley–Queisser theory

[a]*Applied Physics Radiation Technologies Group, CCDCU, School of Engineering and Technology, Sunway University, 47500 Bandar Sunway, Selangor, Malaysia*
[b]*Faculty of Graduate Studies, Daffodil International University, Daffodil Smart City, Birulia, Savar, Dhaka 1216, Bangladesh. E-mail: mayeenk@diu.edu.bd*
[c]*Department of Physics, College of Science, Korea University, 145 Anam-ro, Seongbuk-gu, Seoul, 02841, Republic of Korea*
[d]*Department of Radiological Sciences, College of Applied Medical Sciences, Taif University, P. O. Box 2425, Taif 21944, Saudi Arabia. E-mail: ha.osman@tu.edu.sa*
[e]*Physics Department, Faculty of Science, University of Tabuk, Tabuk, Saudi Arabia. E-mail: sh_issa@ut.edu.sa*
[f]*Department of Physics, Chittagong University of Engineering and Technology, Chattogram 4349, Bangladesh. E-mail: mohi@cuet.ac.bd*
[g]*Department of Physics, American International University-Bangladesh, 408/1, Kuratoli, Khilkhet, Dhaka 1229, Bangladesh. E-mail: habib583@aiub.edu*
[h]*Department of Chemistry, Faculty of Science, Northern Border University, Arar, 91431, Saudi Arabia. E-mail: hajir.wahbi@nbu.edu.sa*
[i]*Ural Federal University, Ekaterinburg 620002, Russia. E-mail: mokhamed.khanfi@urfu.ru*
[j]*Nuclear Materials Authority, P. O. Box 530, El-Maadi, Cairo, Egypt*

predicts a maximum PCE of 33% for materials with bandgaps between 1.2 and 1.4 eV, aligning well with the characteristics of A_3MX_3 perovskites.[16–18] Inorganic lead halide perovskites (ILHPs) are particularly suited for optoelectronic and photovoltaic uses. However, their relatively large bandgaps pose challenges to achieving optimal PCE.[19,20] Recent research highlights the necessity of tuning the bandgap to optimize efficiency. Promising approaches include strain engineering and compositional size tampering, both of which have been shown to effectively reduce the bandgap and enhance PV performance.[21–26] For example, the band structure of lead halide perovskites can fragment, resulting in a significant reduction of approximately 1 eV in the bandgap when spin–orbit coupling (SOC) effects are considered.[27]

Recent studies have demonstrated significant advancements in lead-free perovskite solar cells. For instance, He *et al.* achieved a PCE of 6.53% using novel $MAPbBr_3/CsPbBr_3$ dual absorbers,[28] while Baruah *et al.* developed an inorganic $La_2NiMnO_6/Cs_3Bi_2I_9$ graded absorber architecture with a remarkable PCE of 26.02%.[29] Rahman *et al.* designed a $CdTe/FeSi_3$-based device model, attaining a PCE of 27.35%.[30] In addition to these innovations, tin-halide perovskites have emerged as promising alternatives, offering higher theoretical efficiencies and enhanced carrier mobility.[31] Materials like $NaZnBr_3$ and its variants, such as $NaZn_{0.7}Cu_{0.3}Br_3$, have shown improvements in both stability and efficiency.[32] Furthermore, Ca_3NCl_3 has demonstrated a PCE exceeding 24.73% as an absorber, offering advantages like visible-spectrum absorption, high chemical stability, and environmental friendliness.[33] Although efficiency data for $CaRbCl_3$ remains unreported, both materials show potential for durable, efficient, and scalable solar cell applications, supported by their tunable bandgaps and compatibility with low-temperature manufacturing processes.[33] Recent studies have also emphasized Mg_3SbX_6 (X = I, Br, Cl, F) for its structural stability and direct bandgap, further establishing its potential as a promising material for photovoltaic applications.[34]

First-principles calculations have been extensively utilized to investigate the physical properties of perovskite materials.[35,36] These properties can be tailored by substituting elements,[37] introducing dopants,[38] or applying hydrostatic pressure.[39–41] Linh *et al.*[42] demonstrated that replacing alkali metals with larger ionic radii (*e.g.*, Li, Na, K) in $(Bi_{0.5}M_{0.5})TiO_3$ increased the electronic bandgap. Similarly, Gillani *et al.*[38] showed that doping alkaline earth elements (Mg, Ca, Ba) into $SrZrO_3$ shifted the bandgap from indirect to direct. Hydrostatic pressure is particularly effective in tuning the structural and electronic attributes of A_3BX_3 and ABX_3 perovskites, enabling precise adjustments to their properties for technological applications. This clean and non-invasive approach modifies the crystal structure and electronic characteristics without altering the chemical composition.[43,44] Additionally, the optoelectronic properties of perovskites under varying pressure have been explored,[45,46] highlighting their suitability for p–n junctions, quantum wells, heterostructures, and photovoltaic or optoelectronic devices.[47–50] For instance, Babu *et al.*[51] observed a reduction in the bandgap of $CsSnCl_3$ under compressive pressure, which led to a phase transition from semiconducting to metallic behavior.

Using density functional theory (DFT), this study investigates the physical and optoelectronic properties of novel A_3MX_3 perovskite compounds, specifically Mg_3AB_3 (A = N, Bi; B = F, Cl), for photovoltaic applications. These materials are characterized by their cubic crystal structures, direct bandgaps, and exceptional stability, making them highly promising for next-generation solar cell technologies. The objective of this work is to evaluate their structural, electronic, and optical properties to understand their potential for efficient solar energy conversion. By leveraging first-principles calculations, this study aims to provide insights into the design and optimization of environmentally friendly, lead-free perovskite materials, contributing to sustainable and scalable photovoltaic solutions.

2 Computational technique

In this work first-principles electronic structure calculations were performed using Quantum ESPRESSO software package to gain insights into the structure of Mg_3AB_3 (A = N, Bi; B = F, Br, I) materials. The calculated structure was based on plane-wave pseudopotential method with ultrasoft pseudopotentials were chosen to ensure both the efficiency and the accuracy of the method.[52,53] Exchange-correlation interactions were described within the GGA-PBE approximation, while structural, mechanical, thermal, and vibrational characteristics were investigated in detail. There was a quantitative optimization of the *k*-point sampling, *k*-point mesh of Monkhorst–Pack 10 × 10 × 8 and plane-wave energy respectively 60 Ry to find the best results of all the compounds. For more reliable estimation of energy band and electronic and optical property calculations, the HSE06 hybrid functional was used.[54] Phonon dispersion was investigated using density functional perturbation theory – implemented in the PHONOPY[55] suite for detailed analysis of dynamical stability. The ineffective vibration was studied by employing a supercell (2 × 2 × 2) for the atomic movements of 0.01 Å along the lattice directions. The mechanical stability was estimated by calculating the elastic constants using the energy-strain approach available in the thermo_pw package, implemented within Quantum ESPRESSO.[56,57] These advanced computational methodologies allowed for the detailed study of the structural, mechanical and physical properties of the Mg_3AB_3 (A = N, Bi; B = F, Br, I) compounds to understand if they have the potential for use in state-of-the-art technological applications.

3 Results and discussion

3.1 Structural and thermodynamic stability

The revealed halide perovskite presents the Mg_3AB_3 (A = N, Bi; B = F, Br, I) compounds with the $Pm\bar{3}m$ cubic structure.[58] The unit cell comprises seven atoms: While Mg and A atoms form a face centered cubic cell, the B atoms are situated at the octahedral holes, shown in Fig. 1. The atomic coordinates of these ions are Mg (0.5, 0, 0.5), A (0.5, 0.5, 0.5), B (0, 0, 0.5), which are corresponding to the 3c, 1b, and 3d Wyckoff sites. The variable-cell

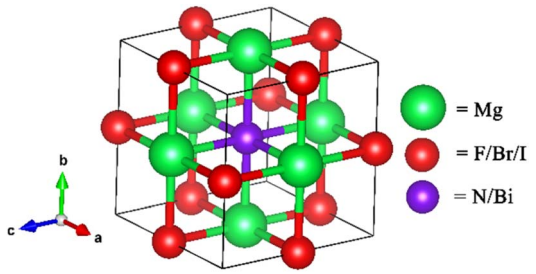

Fig. 1 Unit cell of Mg_3AB_3 (A = N, Bi; B = F, Br, I) compounds.

relaxation (vc-relax) algorithm in Quantum ESPRESSO with projector-augmented wave (PAW) pseudopotentials and the Perdew–Burke–Ernzerhof (PBE) functional showed that the replacement of smaller atoms (N, F) with larger ones (Bi, Br, I) produced uniform lattice expansion through steric effects. The calculated lattice parameters, and the relevant structural information such as lattice constant (a), unit cell volume (V), and formation energy (E_f) are provided in Table 1.

The negative formation energies highlighted that these compounds are thermodynamically stable and energetically favorable for synthesis. The enthalpy of formation (E_f) was computed using the relation:[60]

$$E_f = \frac{E_{total} - \left(xE^{Mg}_{solid} + yE^{A}_{solid} + zE^{B}_{solid}\right)}{x + y + z} \quad (1)$$

Here, x, y and z are the numbers of Mg, A (N/Bi) and B (F/Br/I) at end in the unit cell respectively. The stability of these compounds is further evidenced by negative E_f values, which implies that these compounds are indeed viable for experimental synthesis.

Our simulation confirms the phase stability by connecting cohesive energy analysis with thermodynamic stability. Materials science defines cohesive energy as the amount of energy needed to separate substances into atomic or molecular components.[61,62] This has been determined using the following eqn (1):

$$E^{Mg_3AB_3}_{coh} = \frac{\left(xE^{Mg}_{solid} + yE^{A}_{solid} + zE^{B}_{solid}\right) - E_{total}}{x + y + z} \quad (2)$$

In this case, $E^{Mg_3AB_3}_{coh}$ is the cohesive energy of the Mg_3AB_3 phases, and xE^{Mg}_{solid}, yE^{A}_{solid}, and zE^{B}_{solid} are the sum of the energies of the individual isolated atoms, namely Mg, N/Bi, and F/Br/I, respectively. In this calculation, we isolated one atom from a cubic unit cell with edge length 16 Å, k sampled the gamma point, and relaxed. Table 1 listed the values of cohesive energies to assess thermodynamic stability. These results are strongly indicated that the predicted compounds XIn_2C_2 should be thermodynamically stable and possibly synthesizable.

We applied the eqn (3)–(6) to calculate the reaction energy to address the limited experimental data on the chemical stability of the Mg_3AB_3 (A = N, Bi; B = F, Br, I) compounds and the synthesized Mg_3NF_3 compound. As reference phases we use Mg_3N_2,[63] MgF_2,[64] Mg_3Bi_2,[65] $MgBr_2$,[66] and MgI_2,[67] and assume plausible chemical reactions similar to those carried out in preparing the original compound Mg_3NF_3.[68] Based on that, we calculate the formation enthalpies of Mg_3N_2, MgF_2, Mg_3Bi_2, $MgBr_2$ and MgI_2, −0.114, −0.922, −0.11, −0.175, and −0.932, respectively. In Table 1, we summarize the final reaction energies of the compounds. We then calculate the stability of Mg_3NF_3 to compare the computed result to the synthesized and stable Mg_3NF_3. All these values show the thermodynamic stability of these compounds and there is no competing phase more stable than this.

$$E_{reac} = \left(2\Delta H^{Mg_3AB_3}_f\right) - \left(\Delta H^{Mg_3(N/Bi)_2}_f + 3\Delta H^{Mg(F/Br/I)_2}_f\right) \quad (3)$$

$$Mg_3N_2 + 3MgF_2 = 2Mg_3NF_3 \quad (4)$$

$$Mg_3Bi_2 + 3MgBr_2 = 2Mg_3BiBr_3 \quad (5)$$

$$Mg_3Bi_2 + 3MgI_2 = 2Mg_3BiI_3 \quad (6)$$

The computed, crystallographic data are summarized in Table 1 and compared with the previous experimental values. A good correlation with the experimental values shows that our calculations are provided with quite a reliable estimation. The replacement of two elements with larger atomic radii in Mg_3NF_3: Bi for N and Br or I for F, led to an increase in the values of the lattice constants and the unit cell volume. Geometrical optimization has been carried out with Quantum ESPRESSO. Furthermore, the negative formation energy, negative reaction energy, and positive cohesive energy values, as tabulated in Table 1, strongly indicate the thermodynamic stability of Mg_3AB_3.

Phonon dispersion analysis was used to assess dynamic stability by the finite displacement method[69] using the PHONOPY program.[70] Structural relaxation was done on a 2 × 2 × 2 supercell with an atomic displacement of 0.01 Å were used perform the relevant calculations. In Fig. 2, the phonon dispersion curves (PDCs) along high symmetrical points (Γ–X–M–Γ–R–X) excluded the negative values of the phonon frequencies for all calculated compounds, thus proving the dynamical stability. With seven atoms per unit cell, the

Table 1 Summarizes the lattice parameters (a), unit cell volume (V), and formation energy (E_f) for Mg_3AB_3 (A = N, Bi; B = F, Br, I) compounds

Compounds	a (Å)	V (Å^3)	E_f	$E^{Mg_3AB_3}_{coh}$	E_{reac}	Ref.
Mg_3NF_3	4.269$^{this\ work}$	77.81$^{this\ work}$	−1.6589	3.221	−0.437	59
	4.212^{exp}	74.75^{exp}				
Mg_3BiBr_3	5.767	191.83	−2.4468	2.109	−1.258	
Mg_3BiI_3	6.069	223.59	−1.9767	1.875	−1.047	

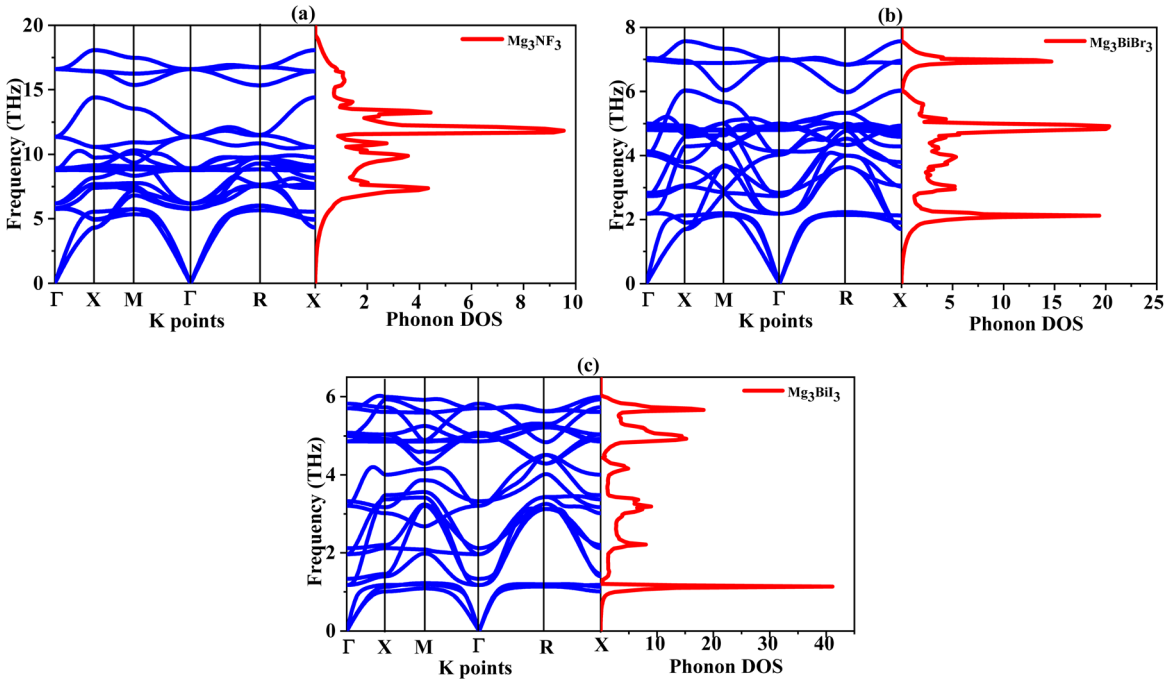

Fig. 2 Phonon dispersion curve with phonon density of state of (a) Mg_3NF_3 (b) Mg_3BiBr_3 (c) Mg_3BiI_3 compounds.

compounds exhibit 21 vibrational modes: 3 acoustic and 18 optical. Acoustic modes with zero frequencies for Γ-point are linear ($\omega = vk$) in the small Q-vector limit. Optical modes can be described as out-of-phase motion of the atomic planes, as opposed to the cooperatively in-phase motion of the planes in acoustic modes. There was not a phonon band gap between the acoustic and lower optical modes as expected from the stability of the vibration. These results give the theoretic foundation for the synthesis of Mg_3AB_3 (A = N, Bi; B = F, Br, I) compounds owing to their structural, and thermodynamically favorable characteristics.

3.2 Mechanical properties

The elastic behavior of a crystal depends expressly on the elastic coefficients that characterize the response of the crystal to applied forces. Knowledge of these properties is necessary when it comes to comprehending mechanical characteristics of the compound. In this research, the mechanical aspect and the elastically related properties of the different compounds were examined using C_{11}, C_{12}, and C_{44} constants. Perovskite compound's mechanical stability was verified based on the criteria: $C_{11} - C_{12} > 0$, $C_{11} + 2C_{12} > 0$ and $C_{44} > 0$. One of the basic properties that determine the character of the material is its strength.[71] Table 2 characterizes the individual elastic coefficients of the investigated compounds.

Thus, for Mg_3AB_3 (A = N, Bi; B = F, B, I) mechanical properties such as bulk modulus (B), shear modulus (G), Young's modulus (Y), Pugh's ratio (B/G), and Poisson's ratio (ν) were predicted. The bulk modulus may be taken to demonstrate the resistance to change in volume at the application of pressure, and the shear modulus describes the connection between shear stress and strain. Yong's modulus calculated from stress-to-strain ratio during uniaxial deformation gives the measure of elasticity of the material.[72,73] The corresponding formulas are given as follows eqn (7)–(11):

$$A = \frac{2C_{44}}{3C_{11} - C_{12}} \quad (7)$$

$$B = \frac{C_{11} + 2C_{12}}{3} \quad (8)$$

$$G = \frac{3C_{44} + C_{11} - C_{12}}{5} \quad (9)$$

$$Y = \frac{9BG}{3B + G} \quad (10)$$

Table 2 Elastic stiffness constant (GPa) and elastic moduli (GPa) for Mg_3AB_3 (A = N, Bi; B = F, Br, I) compounds

Compounds	Mg_3NF_3	Mg_3BiBr_3	Mg_3BiI_3
C_{11}	252.51	76.36	65.09
C_{12}	63.36	18.58	21.42
C_{44}	92.10	22.49	15.81
A	0.265	0.213	0.181
B	126.41	37.84	35.98
G	93.08	24.86	18.00
Y	224.22	61.19	46.28
B/G	1.358	1.522	1.999
ν	0.204	0.230	0.285
B/C_{44}	1.372	1.682	2.274
H_{macro}	16.830	5.016	1.824
H_{micro}	18.374	4.477	2.581

$$v = \frac{3B - Y}{2(3B + G)} \quad (11)$$

The material isotropy was established by using the anisotropy factor (A). They stated that the value of $A = 1.0$ is traditionally used to denote isotropy, and any other numerical value, which departs from this value, indicates anisotropy.[74] Table 2 lists the realistic elastic constants and related parameters. The obtained anisotropy factor (A) values for Mg_3NF_3, Mg_3BiBr_3, and Mg_3BiI_3 are equal to 0.265, 0.213, and 0.181, respectively, proving their anisotropy.

A bulk modulus (B) is a measure of material hardness; a higher value of B of Mg_3NF_3 consistently defines a stronger and harder material than Mg_3BiBr_3 and Mg_3BiI_3. Also, the values of Young's Modulus (Y) and, shear modulus (G) provide information about hardness of materials. In our calculation, we found that both Y and G values are significantly high for Mg_3NF_3, which also indicates its greater hardness compared to the other two compounds.

For determination of ductility/brittleness, absolute Poisson's ratio (v) is used and for it value more than 0.26 suggests ductile material. Among the compounds, Mg_3NF_3 and Mg_3BiBr_3 exhibit brittle nature, whereas Mg_3BiI_3 shows ductile behavior (Table 2).[75] The B/G ratio is also used in the classification of malleability or brittleness. A ratio higher than 1.75 is indicative of ductility as opposed to brittleness for a lesser value of that ratio. According to the B/G ratios, Mg_3NF_3 and Mg_3BiBr_3 materials are brittle in nature while Mg_3BiI_3 is ductile in nature.[76,77]

The machinability index, obtained as B/C_{44}, is a major factor in mechanical performance.[78] Low shear resistance and a smaller C_{44} rating usually equate to enhanced machinability. For example, Mg_3BiI_3 has better machinability properties as compared to the other compounds.

To evaluate hardness, parameters H_{Miao} and H_{Chen} were computed using the following formulas:[79,80]

$$H_{Miao} = \frac{(1 - 2v)Y}{6(1 + v)} \quad (12)$$

and

$$H_{Chen} = 2\left[\left(\frac{G}{B}\right)^2 G\right]^{0.585} - 3 \quad (13)$$

Chen's characterization of superhard materials reveals that the hardness of such material is always greater than 40 GPa. However, as shown in Table 2, the H_{Chen} calculated for Mg_3NF_3, Mg_3BiBr_3 and Mg_3BiI_3 reveal that those materials cannot be referred to as superhard. In both formulas, the hardness values indicate that Mg_3NF_3 is harder than the other two, while Mg_3BiI_3 exhibits the lowest hardness.

The Debye temperature (Θ_D) in the lattice vibration theory corresponds to Fermi's temperature in the metal electronic theory.[81] This essential parameter is closely associated with many thermal and physical properties of materials including elastic coefficients, specific heat and melting point. It is therefore important to understand Θ_D to evaluate how suitable material is for electronic applications.

One widely used method to calculate the Debye temperature involves elastic constant data, with Θ_D determined by averaging the sound velocity, v_m, as expressed by the eqn (14):[82]

$$\Theta_D = \frac{h}{k_B}\left[\left(\frac{3n}{4\pi}\right)N_A\rho/M\right]V_m \quad (14)$$

Here k_B is Boltzmann constant, h is Planck constant, ρ is material density while N_A is Avogadro number, n is number of atoms per molecule and M is molecular weight. The average sound velocity v_m is computed using eqn (15):

$$v_m = \left[\frac{1}{3}\left(\frac{1}{v_l^3} + \frac{2}{v_t^3}\right)\right]^{-1/3} \quad (15)$$

In this equation, v_t and v_l are the transverse and longitudinal sound velocities, respectively, which can be derived from Navier's eqn (16) and (17):[83]

$$v_l = [(3B + 4G)/3\rho]^{1/2} \quad (16)$$

and

$$v_t = [G/\rho]^{1/2} \quad (17)$$

where B is the bulk modulus and G is shear modulus.

With these relations, the Debye temperature, sound velocities (v_t, v_l, v_m), and density (ρ) were computed for Mg_3AB_3 and the data is presented in Table 3. From the above result, the longitudinal velocity is invariably higher than other velocities because it is associated to particle displacements along the direction of wave travel for longitudinal waves. For our calculated compounds Mg_3NF_3, Mg_3BiBr_3, and Mg_3BiI_3, it is ascertained that with an increase in atomic mass the calculated values of Debye temperature are getting down in the range of 804.67 K to 200.09 K. These changes in Θ_D are as a result of differences in the elastic stiffness and bonding strength of the materials used. Debye temperature is very much related to hardness of the material which in turn supports the earlier hardness calculations.[84] The Debye temperature measures the vibrational behavior of lattices in materials. The materials with lower Debye temperatures present softer lattice structures that contribute to enhanced stress tolerance which enables better accommodation of thermal expansion and contraction strains. Materials with lower Debye temperature tend to exhibit reduced thermal conductivity. Heat transport becomes an issue when materials exhibit lower Debye temperature values despite having better mechanical strain accommodation.[85] Mg_3NF_3 showing high Debye temperature characterize high hardness while Mg_3BiI_3 showing low Debye temperature characterizes

Table 3 Calculated density of unit cell (ρ), average (v_m), transverse (v_t), longitudinal (v_l) sound velocities and Debye temperature (Θ_D) of Mg_3AB_3 (A = N, Bi; B = F, Br, I) compounds

Compounds	ρ (kg m^{-3})	v_m (m s^{-1})	v_t (m s^{-1})	v_l (m s^{-1})	Θ_D (K)
Mg_3NF_3	3070.62	5935.77	5374.16	8816.48	804.67
Mg_3BiBr_3	4436.64	2599.41	2346.66	3965.44	256.69
Mg_3BiI_3	4920.20	2132.41	1912.53	3491.27	200.09

low hardness. The low Debye temperatures of Mg_3BiBr_3 and Mg_3BiI_3 suggest enhanced lattice flexibility, enabling better resistance to thermal stress and reducing the risk of micro-cracks during thermal cycling. This property, along with potentially lower thermal conductivity, could improve the device reliability and stability under prolonged operational conditions. Due to the lack of experimental data of these compounds, computational outcomes are anticipated to be further validated *via* experimental analysis.

3.3 Electronic properties

The fundamental electronic structures, including band structures, charge density and density of states (DOS) gives an insight to the electrical behavior of materials.[86] In the present research, analysis of the electronic band structure along high-symmetry directions of the Mg_3AB_3 (A = N, Bi; B = F, Br, I) perovskite structures have been carried out. The band structure plots presented in Fig. 3(a)–(c) are referenced with the Fermi level set to 0 V, enabling a precise comparison of the bandgaps. The band structure is shown along the high symmetry directions of the Brillouin zone for Mg_3AB_3, including the $\Gamma \rightarrow X \rightarrow M \rightarrow \Gamma \rightarrow R \rightarrow X$ paths for the cubic structure. As seen in Fig. 3(a), Mg_3NF_3 shows the direct bandgap where the CBM and VBM are at Γ-point. On the other hand, Fig. 3(b) and (c) depicts that for Mg_3BiBr_3 and Mg_3BiI_3, the CBM is situated at Γ point but the VBM of both materials is slightly lower than that of Γ than R. This arrangement results in an indirect bandgap that is very close to a direct bandgap character for these compounds.

The GGA predicted bandgap for Mg_3NF_3, Mg_3BiBr_3 and Mg_3BiI_3 compounds are presented in Table 4. The band structure calculated using HSE06 is displayed in Fig. 3. From the above compounds, the HSE06 yielded bandgaps of 6.789 eV, 1.626 eV, and 0.867 eV respectively. Semiconductor have band gap rang 0.5–3 eV, while the material with band gap >4 eV is typically classified as strong insulators. By sorting these compounds according to these classifications, the HSE06-calculated bandgap suggests that Mg_3NF_3 is an insulator, while Mg_3BiBr_3 and Mg_3BiI_3 are semiconductors. The omission of SOC may slightly affect the bandgap values, and its inclusion in future studies would provide more precise insights into these properties.

Table 4 Bandgap estimated of Mg_3AB_3 (A = N, Bi; B = F, Br, I) compounds

Compounds	Approach	Nature	Bandgap (eV)	Ref.
Mg_3NF_3	GGA	Direct	3.738	This study
	HSE06	Direct	6.789	This study
Mg_3BiBr_3	GGA	Indirect	1.071	This study
	HSE06	Indirect	1.626	This study
Mg_3BiI_3	GGA	Indirect	0.224	This study
	HSE06	Indirect	0.867	This study

In the analysis of the contribution of specific atomic states on the electronic characteristics of Mg_3AB_3 (A = N, Bi; B = F, Br, I) perovskite structures, the PDOS is quite informative. Note that in Fig. 4(a)–(c) the PDOS distribution is plotted for Mg_3NF_3 in the range of −10 to +15 eV, while for Mg_3BiBr_3 and Mg_3BiI_3, this range is −5 to +8 eV. The total density of states (TDOS) gives general information of the electronic characteristics; the Fermi level (E_F) is revealed by the vertical red dashed line at 0 eV. It is seen that for Mg_3NF_3, the valence band mainly has N-p and F-p orbitals, and the conduction band has Mg-s, p, N-s, p and F-s, p states as depicted in Fig. 4(a). Lack of any kind of electronic states near the Fermi level supports the view of having a large bandgap which defines this material as an insulator. For Mg_3BiBr_3, the valence band is mostly Bi-p and Br-p composition which suggests the substantial mixing between these states (Fig. 4(b)). Mg-p, Bi-p, d and I-p, d orbitals play vital roles in the conduction band and all the three bands are significantly influenced in the conduction band by the electronic transitions. In the case of Mg_3BiI_3 (Fig. 4(c)), the valence band comprises the I-p and Bi-p states with visible mixing between these two bands. It is also clear that Mg-p, Bi-p, d and I-p, d orbitals have contributions to the conduction band implying their relevance for the electronic transitions. These features are characteristic of semiconductors and particularly are suitable for optoelectronics. These analyses demonstrate that the atomic states and the orbital hybridization of electrons are significant for the electronic characteristic of Mg_3AB_3 compounds.

In Fig. 5, the electronic charge density maps of Mg_3AB_3 (A = N, Bi; B = F, Br, I) perovskite compounds are displayed to witness the charge distribution. The shades of colour in the

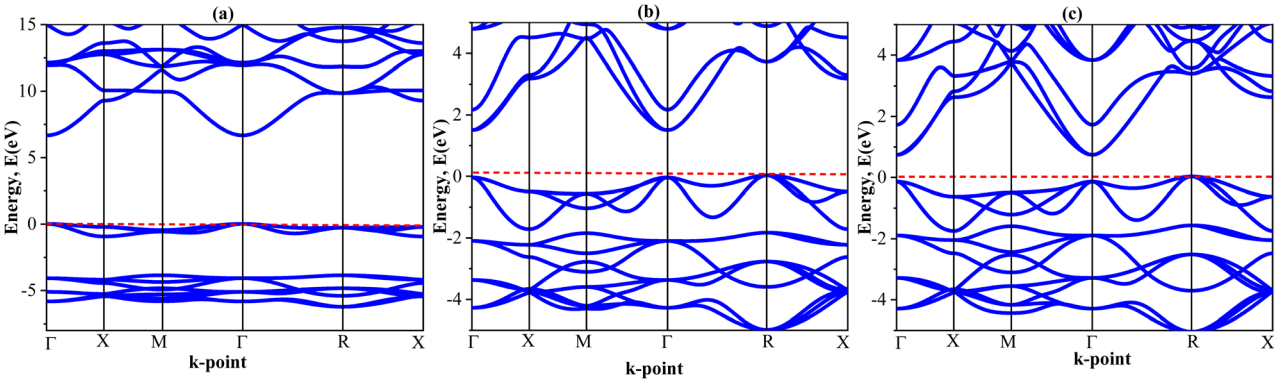

Fig. 3 Band structure of (a) Mg_3NF_3, (b) Mg_3BiBr_3 and (c) Mg_3BiI_3.

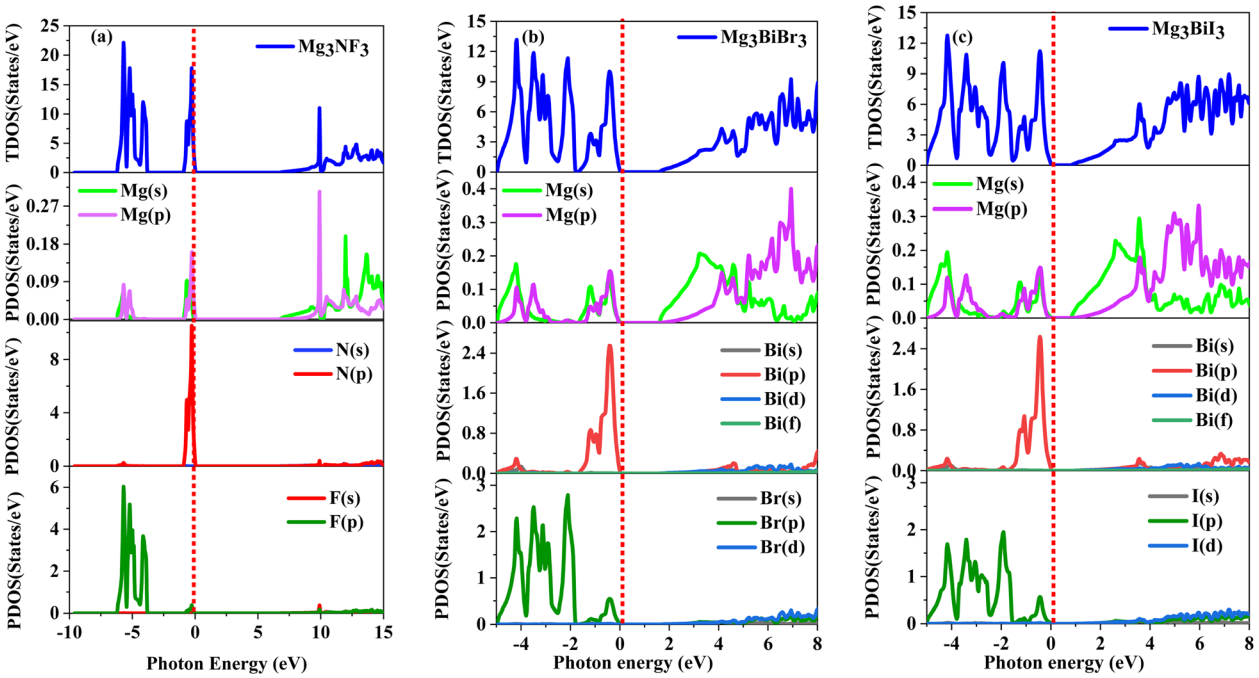

Fig. 4 Total and partials DOS of (a) Mg_3NF_3, (b) Mg_3BiBr_3 and (c) Mg_3BiI_3.

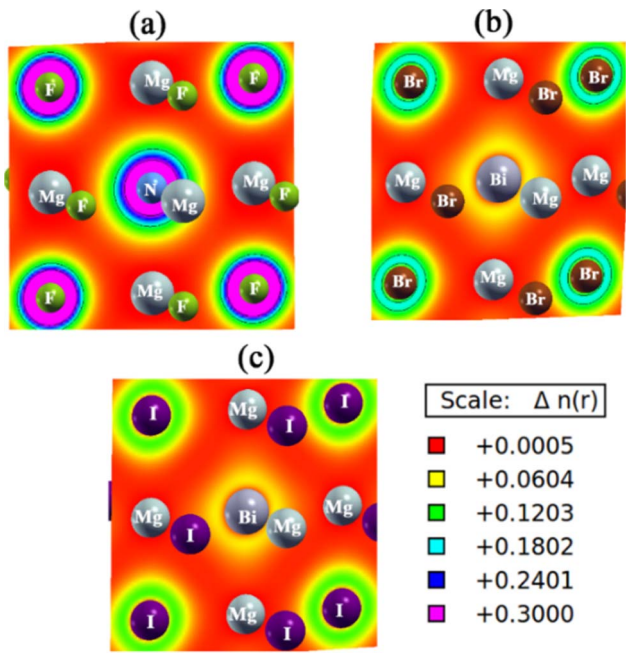

Fig. 5 Electronic charge density of (a) Mg_3NF_3 (b) Mg_3BiBr_3 (c) Mg_3BiI_3 compounds.

maps correspond to the charge density as pointed out by the scale bar at the bottom of each map.

Bonds in Mg_3AB_3 perovskites are ionic and partially covalent depending on charge states of ions (Mg^{2+}, N^{3-} or Bi^{3+} and halogen anions). In turn, magnesium ionized in solution as Mg^{2+}, was participating in bond formation of both nitrogen and bismuth with the valence halogen anion. In compounds of Mg_3BiBr_3 and Mg_3BiI_3, the halide ions have significant contribution for the ionic environment with strong electrostatic interaction with Mg^{2+}, similarly bismuth (Bi^{3+}) also has got very close coordination with Mg^{2+} as it has got high net positive charge.

Bonding characteristics are much influenced by the halogens. Fluorine (F^-) being one of the highest electronegative elements ions very strongly localize electron density around itself, forming dominantly ionic bonds with Mg^{2+}. The ionic radii are larger for bromine (Br^-) and iodine (I^-), which have lower electronegativity and a slightly weaker ionic bond due to more diffuse electron density distribution. But these halides are essential for stabilizing the perovskite structure.

The bonding also includes partial covalent character for compounds that contain bismuth and heavier halogens such as bromine and iodine because of orbital overlap. Iodine is an outcry concern because of its larger size and greater polarizability, which makes it an especially strong covalent interaction. Charge density maps show high electron density around halogens identifying them as ionic, and diffuse charge density around Mg^{2+} because of its role in stabilizing this complex. Stability and electronic properties of these materials arise from the balance of ionic and covalent interactions.

3.4 Optical properties

The optoelectronic properties of the Mg_3AB_3 structures (A = N, Bi; B = F, Br, I) are investigated to understand their light absorption, reflectivity, loss function, dielectric properties, and other related properties. The dielectric function $\varepsilon(\omega)$ consists of two components: the real part is denoted by $\varepsilon_1(\omega)$, while the imaginary part is denoted by $\varepsilon_2(\omega)$, and can be represented by eqn (18):

$$\varepsilon(\omega) = \varepsilon_1(\omega) + i\varepsilon_2(\omega) \quad (18)$$

Table 5 Key optical properties of Mg_3AB_3 (A = N, Bi; B = F, Br, I) compounds

Compounds	Mg_3NF_3	Mg_3BiBr_3	Mg_3BiI_3
$\varepsilon_1(0)$	2.029	5.713	6.889
$\varepsilon_{2max}(\omega)$	3.01 (13.16 eV)	7.56 (4.30 eV)	8.706 (3.74 eV)
$\alpha(0)$	6.69 eV	1.65 eV	0.98 eV
$\alpha_{max}(\omega)$	13.25 eV	11.44 eV	9.25 eV
$L(0)$	7.13 eV	3.67 eV	1.45 eV
$R(0)$	2%	16%	20%
$R_{max}(\omega)$	18%	37%	44%
$\sigma_{max}(\omega)$	4.68 (13.14 eV)	4.62 (8.73 eV)	4.95 (7.54 eV)
$n(0)$	1.41	2.39	2.63

It has been calculated by the Kramers–Kronig transformation from the real part and from the momentum matrix elements for the imaginary part.[87]

The calculated $\varepsilon_1(0)$ values are outlined in the Table 5 below. From Fig. 6(c) it is clear that Mg_3NF_3 has a nearly constant response across the full range of photon energy implying weak electronic transitions and case of which is consistent with the insulating property of the compound. On the other hand, Mg_3BiBr_3 and Mg_3BiI_3 exhibit distinct peaks in $\varepsilon_1(\omega)$ indicating significant electronic polarization and moderate interband transition. The first peak of Mg_3BiI_3 occurs around 3.47 eV, slightly higher than that of Mg_3BiBr_3, due to iodine occupying more space and being more polarized than bromine ions. Compared with the halogen parent compound, these results show the differences in dielectric responses owing to halogen substitution. Although Mg_3NF_3 is non-conductive and demonstrates a low level of optical activity, Mg_3BiBr_3 and Mg_3BiI_3 have high levels of optical activity that make them suitable for optoelectronic applications.

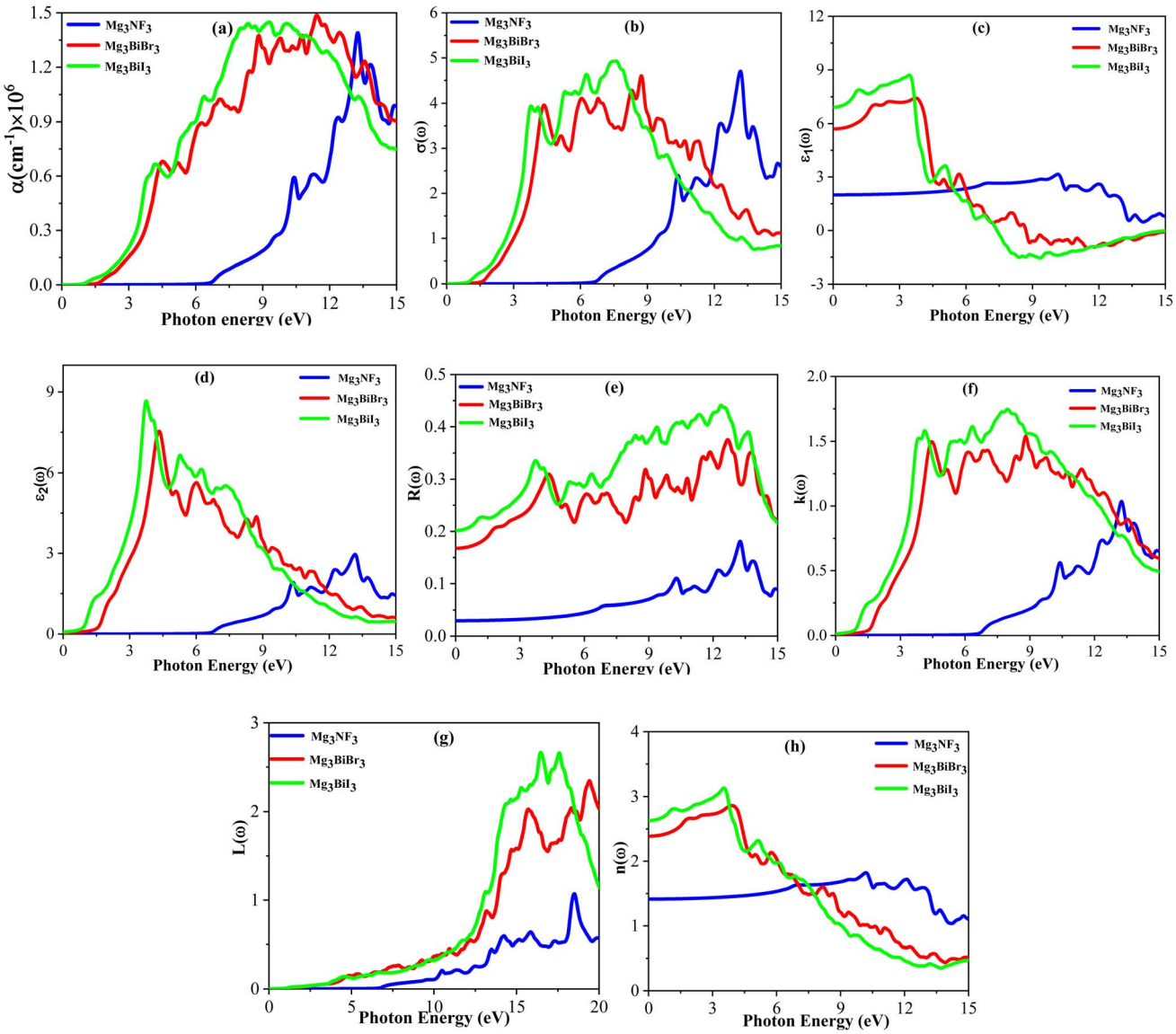

Fig. 6 Calculated optical parameters (a) absorption coefficient, (b) conductivity, (c) real dielectric part, (d) imaginary dielectric part, (e) reflectivity, (f) extinction coefficient, (g) loss function and (h) refractive index of Mg_3AB_3 (A = N, Bi; B = F, Br, I).

$\varepsilon_2(\omega)$, the second component of the dielectric function, is an essential factor in evaluating the ability of light absorption and the energy gain capability. The $\varepsilon_2(\omega)$ for the Mg_3AB_3 structures are presented in Fig. 6(d) where the values corresponding to the highest peak are also given in the Table 5. By observing the imaginary part, it is seen that the particular materials under consideration react to electromagnetic radiation. The imaginary part of dielectric function $\varepsilon_2(\omega)$ indicate that Mg_3NF_3 has low absorption with no major electronic transitions, while Mg_3BiBr_3 and Mg_3BiI_3 exhibit higher absorption levels and a noticeable peak, indicating significant interband absorption. These results demonstrate that Mg_3BiBr_3 and Mg_3BiI_3 are more optically lively compounds that are suitable for potential optoelectronic uses.

The absorption coefficient $\alpha(\omega)$ follows the dependence of $\varepsilon_2(\omega)$. The absorption coefficient of the Mg_3AB_3 compounds is displayed in Fig. 6(a), which is in the range of 10^5 to 10^6 cm^{-1} near the absorption edges, while the static and peak values are given in Table 5, the result showed that Mg_3NF_3 exhibits significantly a lower absorption coefficient, and this is attributed to the insulating nature of Mg_3NF_3. On the other hand, Mg_3BiBr_3 and Mg_3BiI_3 show absorptivity values higher than the previous compounds, which would make them ideal for use in optoelectronic and photovoltaic devices.

The optical conductivity of these compounds, shown in Fig. 6(b), does not take any action below the energy band gap owing to the lack of electronic transitions. However, at higher energy levels above the band gap, the conductance rises drastically owing to photon stimulated excitation of the electrons and mainly due to interband transition. All these calculated compounds exhibit high optical conductivity, with Mg_3BiBr_3 and Mg_3BiI_3 showing comparatively lower conductivity than Mg_3BiI_3.

The reflectivity spectra $R(\omega)$ of the Mg_3AB_3 compounds in Fig. 6(e) indicates different behavior within the photon energies. The low reflectivity of Mg_3NF_3 is in concordance with the insulating nature, whereas Mg_3BiBr_3 and Mg_3BiI_3, which are semiconductors by behavior, have higher reflectivity than Mg_3NF_3, but quite perfect for absorbing materials in solar cell. The static values of optical reflectivity of Mg_3AB_3 compounds are summarized in Table 5 and the highest value is 20% for Mg_3BiI_3. The reflectivity values in the visible spectrum follow the trend: Mg_3NF_3 > Mg_3BiBr_3 > Mg_3BiI_3. The static values of optical reflectivity of Mg_3AB_3 compounds are summarized in Table 5.

In Fig. 6(f) and (h) are depicted the extinction coefficient $k(\omega)$ and the refractive index $n(\omega)$ which describes the amount of incident photons that are absorbed and velocity of light in the material. Static and optical values of the refractive index for Mg_3AB_3 compounds are similar to the real part of the dielectric tensor, which are shown in Table 5. The extinction coefficient persists to be zero at within the energy band gap while the $k(\omega)$ values are high at the higher photon energies representing interband transitions.

The last one, depicted in Fig. 6(g), characterizes the energy loss $L(\omega)$ over the course of the interaction of the electromagnetic radiation with the material. Local maxima of $L(\omega)$ are found to be at 18.49 eV for Mg_3NF_3, at 19.49 eV for Mg_3BiBr_3, and 16.40 eV for Mg_3BiI_3, which are the points of peak energy losses in view of interaction with electrons.

In summary, the properties of the calculated compounds are comparable to those of well-known materials such as $CH_3NH_3PbCl_3$, $CsPbI_3$, and $MAPbCl_3$,[88–90] highlighting their potential as highly efficient materials for photovoltaic energy conversion. Optoelectronic performance in the order of Mg_3BiBr_3 and Mg_3BiI_3 is shown to be excellent, including a high light absorption coefficient and optical conductivity, low optical reflectivity, and a suitable band gap. Finally, their properties make them highly attractive for photovoltaic applications. Overall, the non-toxicity, thermal stability, and mechanical stability of Mg_3AB_3 compounds offer significant advantages, highlighting their potential for use in environmentally friendly optoelectronic devices. In future studies, we recommend exploring the light absorption spectra of these materials using advanced methods, such as the Bethe–Salpeter Equation (BSE) combined with the GW method, to achieve more precise results.[91–93]

3.5 Thermal properties

The thermal properties of Mg_3AB_3 (A = N, Bi; B = F, Br, I), such as lattice thermal conductivity, melting temperature, minimum of thermal conductivity, and Grüneisen parameters are investigated, which give a clear understanding of thermal characteristics. In cubic crystals like the perovskite structure, the melting temperature can be predicted using the empirical formula developed by Fine *et al.*,[94] which depends on the single crystal elastic constant:

$$T_m(K) = 553 + (5.911)C_{11} \quad (19)$$

The calculated melting temperatures for Mg_3AB_3 (A = N, Bi; B = F, Br, I) are given in Table 6 below where it is observed that all the compounds exhibit a decreasing trend in their melting temperatures as the composition varies. The thermal conductivity of a system depends on atomic interactions, and the minimum thermal conductivity represents the theoretical lower limit of intrinsic thermal conductivity, calculated using the formula:[95]

$$K_{min} = K_B V_m \left(\frac{M}{n\rho N_A}\right)^{-\frac{2}{3}} \quad (20)$$

We have obtained that the minimum of the thermal conductivity of Mg_3BiB_3 and Mg_3BiI_3 is lower than that of Mg_3NF_3. Thermal conductivity is another material property that has to be low when it comes to application in coatings for thermal protection which are called thermal barrier coatings (TBC).

For perovskite materials, knowledge of the lattice thermal conductivity K_{ph} is critical because it is implicated in heat dissipation and device efficiency. The empirical Slack model, which is valid for applications involving crystalline materials

Table 6 Calculated Grüneisen parameter (γ), specific heat (C_v, C_p), minimum thermal conductivity (K_{min}), lattice thermal conductivity (K_{ph}), and melting temperature (T_m) of Mg_3AB_3 (A = N, Bi; B = F, B, I) perovskite compounds

Compounds	γ	C_p (J mol^{-1} K^{-1})	C_v (J mol^{-1} K^{-1})	K_{min} (W m^{-1} K^{-1})	K_{ph} (W m^{-1} K^{-1})	T_m (K)
Mg_3NF_3	1.301	89.45	89.22	1.64	75.51	2045.633
Mg_3BiBr_3	1.408	120.86	120.21	0.39	9.92	1004.421
Mg_3BiI_3	1.683	123.83	121.87	0.29	4.36	937.761

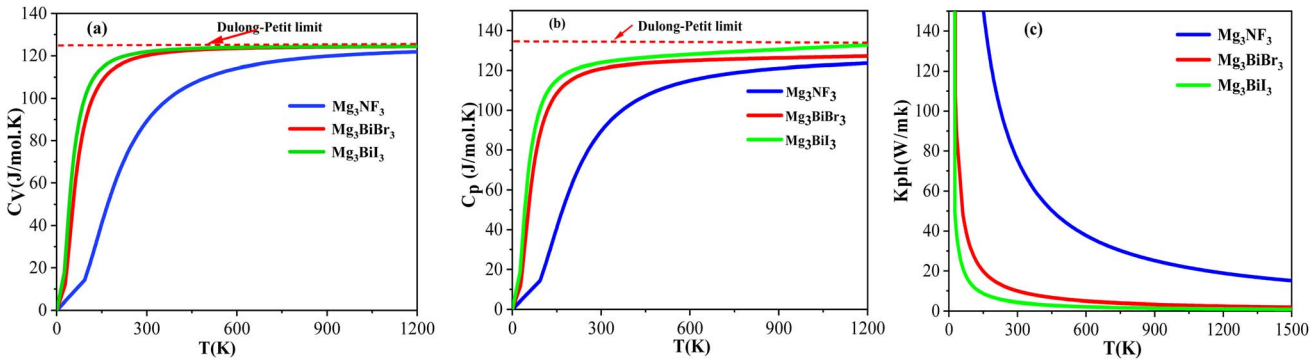

Fig. 7 The temperature-dependent specific heats (a) C_v at constant volume (b) C_p at constant pressure and (c) lattice thermal conductivity of Mg_3AB_3 (A = N, Bi; B = F, Br, I) perovskite compounds.

where phonon edge scattering controls thermal conduction, is used to determine K_{ph}. The formula is:[96]

$$K_{ph} = A(\gamma)\frac{M_{av}\Theta_D{}^3}{\gamma^2 n^{2/3} T} \quad (21)$$

where M_{av} is the average atomic mass, n is the number of atoms per unit cell, T is the temperature, γ is the Grüneisen parameter, and $A(\gamma)$ is a factor that acts in proportion with the Grüneisen parameter. System with higher Grüneisen parameter is more anharmonic in nature and possess low phonon thermal conductivity.

As seen in Table 6, the Grüneisen parameter for all Mg_3AB_3 compounds is moderate. The estimates of lattice thermal conductivity of Mg_3AB_3 perovskite phases at 300 K are presented in Table 6, whereas the dependence on T is shown in Fig. 7.

The lattice thermal conductivity of all three compound decreases with increasing temperature; however, K_{ph} for Mg_3NF_3 starts at a much higher value and decreases slowly with temperature; Mg_3BiBr_3 and Mg_3BiI_3, on the other hand, experience a relatively steeper drop at low temperatures. As for the K_{ph}, it is increased with the increasing of temperature but not as much as the initial values of Mg_3NF_3.

A thermal property of metal is specific heat whereby variation has a profound effect on casting and heat treatment among other operations as it defines the heat needed. Heat capacity is a thermodynamic property that quantifies the amount of heat required to change the temperature of a material by a given amount. When heat is supplied to a substance, the temperature of the material rises to levels corresponding to the heat. Fig. 7(b) and (c) depicts the C_v and C_p of states at the temperature range of 0 to 1200 K. The result of the increase in certain heat with temperature is thermal softening. Like for Mg_3BiBr_3 and Mg_3BiI_3, the C_v and C_p rise steeply in the 0–100 K range and for Mg_3NF_3 at the 0–900 K range. The high-temperature values are close to Dulong Petit (DP) limit but lower than Dulong Petit limit at all temperatures with the exception of the lowest one. Compared with C_p, the DP model[97,98] predicts slightly lower C_p at high temperatures by 2.9–3.9% at 1200 K. Such behavior associates this material with conventional solids, were anharmonic effects impact C_p at elevated temperatures. The heat capacity values at 300 K are given in the Table 6. Based on the computations we did, Mg_3NF_3 has relatively low phonon mean free path and substantial lattice thermal conductivity and a high melting temperature meaning that it can effectively be used as heat sink material. These properties are similar to those of Ti_2BC,[99] another material that is believed to act as a good heat sink. On the other hand, while the minimum thermal conductivity (K_{min}) values of the Mg_3BiI_3 and Mg_3BiBr_3 are low, they can be apt for use as thermal barrier coating (TBC) materials, however further experimental and details study need to fully understand these applications. The obtained K_{min} values correlate well with the K_{min} of other reference TBC materials, $Y_4Al_2O_9$ (ref. 100) and Yb_2SiO_5.[101] This similarity further highlights their usefulness in the high-temperature systems where effective thermal protection is needed.

4 Conclusion

The structural, mechanic, electrical, optical, and thermal characteristics of Mg_3AB_3 (A = N, Bi; B = F, Br, I) perovskite have been investigated employing density functional theory (DFT). Both structural and thermodynamic studies substantiate the stability of these materials. Mechanical characterization from analysis shows that Mg_3BiI_3 is very ductile and easy to work

while, Mg_3BiBr_3 and Mg_3BiI_3 are more brittle with moderate hardness. Band structure electronic calculations show that Mg_3NF_3 has a wide direct band gap that qualifies it as an insulator whereas Mg_3BiBr_3 and Mg_3BiI_3 possess indirect bandgaps suitable for semiconductor optoelectronic devices. While indirect bandgaps can result in slightly lower absorption efficiency compared to direct bandgap materials, many successful photovoltaic materials, like silicon, also have indirect bandgaps and perform well. The bandgaps of Mg_3BiI_3 (0.867 eV) and Mg_3BiBr_3 (1.626 eV) fall outside the ideal range for single-junction solar cells (1.1–1.4 eV) but still allow for efficient photon absorption and energy conversion, with Mg_3BiBr_3 being closer to the optimal range. These bandgaps make Mg_3BiI_3 a potential bottom cell material in tandem solar cells, while Mg_3BiBr_3, being near the ideal limit, could contribute to enhanced efficiency. The optical analysis for Mg_3NF_3 shows low conductivity because of the insulating properties, in contrast, Mg_3BiBr_3 and Mg_3BiI_3 exhibit significant light-harvesting capabilities due to their pronounced interband transitions, high absorption coefficient, moderate reflectivity, relatively high conductivity and reduced optical losses, which underscoring their suitability for optoelectronic devices, particularly solar cells. Thermal characterization studies place Mg_3NF_3 as a candidate for heat sink applications while Mg_3BiBr_3 and Mg_3BiI_3 with low thermal conductivity are suitable for thermal barrier coatings. These compounds appear to offer high optical activity, suitable electronic band gaps and chemical stability. Unlike traditional lead-based perovskites, Mg_3AB_3 compounds are environmentally friendly and renewable which makes their usage more suitable in the future generations of solar cells. This work highly recommends the use of Mg_3BiB_3 and Mg_3BiI_3 in photovoltaic technologies due to their high absorption, low reflectivity, and closeness to the ideal bandgap incurred in photovoltaic applications. Therefore, further research is needed to validate such techniques and to explore how the applicability of these techniques might be promoted.

Consent for publication

All authors of this work have agreed and are ready to sign the transfer of copyright which empowers the publisher to protect the work against unauthorized use and to maintain the integrity of the work from a bibliographical and archival standpoint.

Data availability

All data are available in the manuscript.

Author contributions

Mayeen Uddin Khandaker and M. M. Uddin: conceptualization, writing of original draft, and reviewing and editing of the manuscript; Hamid Osman and Shams Issa: simulation, software and validation, and writing of original draft, Md. Habib Ullah, Hajir Wahbi and M. Y. Hanfi: model calculation, discussion and validation, and reviewing of the manuscript.

Conflicts of interest

The authors declare that they have no known competing financial interests or personal relationships that could have appeared to influence the work reported in this paper.

Acknowledgements

The authors extend their appreciation to the Deanship of Scientific Research at Northern Border University, Arar, KSA for funding this research work through project number "NBU-FFR-2025-2916-04". During the preparation of this work, the authors used some online services (Gemini, Grammarly) to improve language and readability. After using this tool/service, the authors reviewed and edited the content as needed and took full responsibility for the content of the publication.

References

1 K. Liu, B. Chen, Z. J. Yu, Y. Wu, Z. Huang, X. Jia, *et al.*, Reducing sputter induced stress and damage for efficient perovskite/silicon tandem solar cells, *J. Mater. Chem. A*, 2022, **10**, 1343–1349, DOI: 10.1039/D1TA09143C.

2 J. P. Thomas and K. T. Leung, Defect-Minimized PEDOT:PSS/Planar-Si Solar Cell with Very High Efficiency, *Adv. Funct. Mater.*, 2014, **24**, 4978–4985, DOI: 10.1002/adfm.201400380.

3 A. Hossain, M. A. Ali, M. M. Uddin, S. H. Naqib and M. M. Hossain, Theoretical studies on phase stability, electronic, optical, mechanical and thermal properties of chalcopyrite semiconductors $HgXN_2$ (X=Si, Ge and Sn): A comprehensive DFT analysis, *Mater. Sci. Semicond. Process.*, 2024, **172**, 108092, DOI: 10.1016/j.mssp.2023.108092.

4 J. P. Wilcoxon, G. A. Samara and P. N. Provencio, Optical and electronic properties of Si nanoclusters synthesized in inverse micelles, *Phys. Rev. B:Condens. Matter Mater. Phys.*, 1999, **60**, 2704–2714, DOI: 10.1103/PhysRevB.60.2704.

5 A. Kojima, K. Teshima, Y. Shirai and T. Miyasaka, Organometal Halide Perovskites as Visible-Light Sensitizers for Photovoltaic Cells, *J. Am. Chem. Soc.*, 2009, **131**, 6050–6051, DOI: 10.1021/ja809598r.

6 S. D. Stranks, G. E. Eperon, G. Grancini, C. Menelaou, M. J. P. Alcocer, T. Leijtens, *et al.*, Electron-Hole Diffusion Lengths Exceeding 1 Micrometer in an Organometal Trihalide Perovskite Absorber, *Science*, 2013, **342**, 341–344, DOI: 10.1126/science.1243982.

7 G. E. Eperon, S. D. Stranks, C. Menelaou, M. B. Johnston, L. M. Herz and H. J. Snaith, Formamidinium lead trihalide: a broadly tunable perovskite for efficient planar heterojunction solar cells, *Energy Environ. Sci.*, 2014, **7**, 982–988, DOI: 10.1039/C3EE43822H.

8 M. R. Sabour, M. A. Jafari and S. M. Hosseini Gohar, Si-based Solar Cells' Conversion Efficiency Related Publications Bibliometric Review During 2000-2017, *Silicon*, 2020, **12**, 2705–2720, DOI: 10.1007/s12633-019-00366-4.

9 F. Hao, C. C. Stoumpos, D. H. Cao, R. P. H. Chang and M. G. Kanatzidis, Lead-free solid-state organic–inorganic halide perovskite solar cells, *Nat. Photonics*, 2014, **8**, 489–494, DOI: 10.1038/nphoton.2014.82.

10 S. Niu, H. Huyan, Y. Liu, M. Yeung, K. Ye, L. Blankemeier, T. Orvis, D. Sarkar, D. J. Singh, R. Kapadia and J. Ravichandran, Band-Gap Control via Structural and Chemical Tuning of Transition Metal Perovskite Chalcogenides, *Adv. Mater.*, 2017, **29**, 1604733, DOI: 10.1002/adma.201604733.

11 A. Ghosh, M. F. Rahman, M. R. Islam, M. S. Islam, M. Amami, M. K. Hossain and A. B. M. Ismail, *Heliyon*, 2023, **9**(8), e19271, DOI: 10.1016/j.heliyon.2023.e19271.

12 Md. S. Islam, Md. F. Rahman, Md. R. Islam, A. Ghosh, Md. A. Monnaf, Md. S. Reza, *et al.*, An in-depth analysis of how strain impacts the electronic, optical, and output performance of the Ca_3NI_3 novel inorganic halide perovskite, *J. Phys. Chem. Solids*, 2024, **185**, 111791, DOI: 10.1016/j.jpcs.2023.111791.

13 Md. F. Rahman, Md. H. Rahman, Md. R. Islam, M. K. Hossain, A. Ghosh, Md. S. Islam, *et al.*, The optical and electronic properties of inorganic halide perovskite Sr3NCl3 under applied biaxial strain, *J. Mater. Sci.*, 2023, **58**, 13100–13117, DOI: 10.1007/s10853-023-08825-5.

14 Md. S. Islam, Md. F. Rahman, Md. R. Islam, Q. Mahmood, M. m. Al-Anazy, Md. Z. Hasan, *et al.*, Investigation strain effects on the electronic, optical, and output performance of the novel inorganic halide perovskite Sr_3SbI_3 solar cell, *Chin. J. Phys.*, 2024, **88**, 270–286, DOI: 10.1016/j.cjph.2024.01.011.

15 M. A. B. Shanto, M. F. Rahman, M. R. Islam, A. Ghosh, A. Azzouz-Rached, H. Albalawi, *et al.*, Investigating how the electronic and optical properties of a novel cubic inorganic halide perovskite, Sr_3NI_3 are affected by strain, *F1000Research*, 2023, **12**, 1005, DOI: 10.12688/f1000research.137044.1.

16 A. Ghosh, Md. Ferdous Rahman, A. Kuddus, M. K. A. Mohammed, Md. Rasidul Islam, S. Bhattarai, *et al.*, Investigating of novel inorganic cubic perovskites of A_3BX_3 (A=Ca, Sr, BP, As, X=I, Br) and their photovoltaic performance with efficiency over 28%, *J. Alloys Compd.*, 2024, **986**, 174097, DOI: 10.1016/j.jallcom.2024.174097.

17 A. Ghosh, M. F. Rahman, M. R. Islam, M. S. Islam, M. K. Hossain, S. Bhattarai, *et al.*, Structural, electronic and optical characteristics of inorganic cubic perovskite Sr_3AsI_3, *Opt. Continuum*, 2023, **2**, 2144–2153, DOI: 10.1364/OPTCON.495816.

18 M. F. Rahman, M. Harun-Or-Rashid, M. R. Islam, A. Ghosh, M. K. Hossain, S. Bhattarai, *et al.*, Exploring the impact of strain on the electronic and optical properties of inorganic novel cubic perovskite Sr3PI3, *Phys. Scr.*, 2023, **98**, 115105, DOI: 10.1088/1402-4896/acfce9.

19 M. A. Green, Y. Jiang, A. M. Soufiani and A. Ho-Baillie, Optical Properties of Photovoltaic Organic–Inorganic Lead Halide Perovskites, *J. Phys. Chem. Lett.*, 2015, **6**, 4774–4785, DOI: 10.1021/acs.jpclett.5b01865.

20 J. Deng, J. Li, Z. Yang and M. Wang, All-inorganic lead halide perovskites: a promising choice for photovoltaics and detectors, *J. Mater. Chem. C*, 2019, **7**, 12415–12440, DOI: 10.1039/C9TC04164H.

21 S. Bouhmaidi, R. K. Pingak and L. Setti, First-principles investigation of electronic, elastic, optical and thermoelectric properties of strontium-based anti-perovskite Sr_3MN (M= P and As) for potential applications in optoelectronic and thermoelectric devices, *Moroccan J. Chem.*, 2023, **11**(4), 1254–1265, DOI: 10.48317/IMIST.PRSM/morjchem-v11i04.41366.

22 A. Sedky, A. Hakamy, N. Afify, S. Bouhmaidi, L. Setti, D. Hamad, *et al.*, Comparative investigation of structural, photoluminescence, and magnetic characteristics of $M_xSn_{1-x}O_y$ nanocomposites, *Appl. Phys. A*, 2023, **129**, 669, DOI: 10.1007/s00339-023-06941-2.

23 J. Qian, B. Xu and W. Tian, A comprehensive theoretical study of halide perovskites ABX_3, *Org. Electron.*, 2016, **37**, 61–73, DOI: 10.1016/j.orgel.2016.05.046.

24 P. Ramasamy, D.-H. Lim, B. Kim, S.-H. Lee, M.-S. Lee and J.-S. Lee, All-inorganic cesium lead halide perovskite nanocrystals for photodetector applications, *Chem. Commun.*, 2016, **52**, 2067–2070, DOI: 10.1039/C5CC08643D.

25 G. Nawab, A. U. Rahman, I. U. Haq, A. Ali, A. Abdelkader, A. H. Ismail, *et al.*, Structural and optoelectronic properties of 2D halide perovskites Cs_2MBr_4 (M = Zn, Cd, Hg): a first principle study, *Opt. Quantum Electron.*, 2024, **56**, 871, DOI: 10.1007/s11082-024-06710-2.

26 I. U. Haq, A. Ali, A. AbdelKader, A. H. Ismail, M. Alomar and I. Khan, Ground state structure and optoelectronic properties of novel quasi-2D layered halide perovskites $CsPb_2X_5$ (X= Cl, Br, I) via first principle calculations, *Mater. Sci. Semicond. Process.*, 2024, **176**, 108326, DOI: 10.1016/j.mssp.2024.108326.

27 M. Pandey, K. W. Jacobsen and K. S. Thygesen, Band Gap Tuning and Defect Tolerance of Atomically Thin Two-Dimensional Organic–Inorganic Halide Perovskites, *J. Phys. Chem. Lett.*, 2016, **7**, 4346–4352, DOI: 10.1021/acs.jpclett.6b01998.

28 B. He, L. Liu, J. Hu, S. Nie, Y. Chen and Y. Chen, The properties of perovskite solar cells with novel $MAPbBr_3$/$CsPbBr_3$ double absorber, *J. Phys. D: Appl. Phys.*, 2022, **56**, 015107, DOI: 10.1088/1361-6463/ac9ce5.

29 S. Baruah, J. Borah, B. Vandana, S. Simran, M. Nagendra and S. Rajasekaran, Improvement of photovoltaic response in perovskite solar cell via all inorganic lead free cubic double La_2NiMnO_6/Cs3Bi2I$_9$ based graded absorber architecture, *Opt. Quantum Electron.*, 2024, **56**, 1321, DOI: 10.1007/s11082-024-07239-0.

30 Md. F. Rahman, M. J. A. Habib, Md. H. Ali, M. H. K. Rubel, Md. R. Islam, A. B. Md. Ismail, *et al.*, Design and numerical investigation of cadmium telluride (CdTe) and iron silicide ($FeSi_2$) based double absorber solar cells to enhance power conversion efficiency, *AIP Adv.*, 2022, **12**, 105317, DOI: 10.1063/5.0108459.

31 M. Roknuzzaman, K. Ostrikov, H. Wang, *et al.*, Towards lead-free perovskite photovoltaics and optoelectronics by

ab-initio simulations, *Sci. Rep.*, 2017, **7**, 14025, https://www.nature.com/articles/s41598-017-13172-y.

32 M. E. Emetere, O. O. Bello and S. A. Afolalu, Enhancement of novel $NaZnBr_3$ perovskite for solar cells application, *Energy Rep.*, 2022, **8**, 4453–4460, DOI: 10.1016/j.egyr.2022.03.087.

33 M. Sadia Islam Ria, A. Ghosh, Md. Azizur Rahman, J. Y. Al-Humaidi, N. S. Awwad, H. A. Ibrahium, *et al.*, Examining anion influence on the physical properties and performance analysis of lead-free calcium-based Ca_3NX_3 (X=F, Cl, Br and I) perovskite, *Mater. Sci. Eng., B*, 2024, **310**, 117674, DOI: 10.1016/j.mseb.2024.117674.

34 I. K. G. G. Apurba, M. R. Islam, M. S. Rahman, M. F. Rahman and S. Ahmad, Exploring the inorganic perovskite materials Mg_3SbX_3 (Where, X=I, Br, Cl and F) through the perspective of density functional theory: Adjustment of physical characteristics as consequence of strain, *Heliyon*, 2024, **10**(20), e39218, DOI: 10.1016/j.heliyon.2024.e39218.

35 A. Hosen, Md. A. Hossain, M. S. Abu-Jafar, R. K. Pingak and A. A. Mousa, Unraveling lead-free Fr-based perovskites $FrQCl_3$ (Q = Ca, Sr) and their pressure induced physical properties: DFT analysis for advancing optoelectronic performance, *J. Phys. Chem. Solids*, 2024, **193**, 112211, DOI: 10.1016/j.jpcs.2024.112211.

36 H. Akter, M. A. Ali, M. M. Hossain, M. M. Uddin and S. H. Naqib, Oxysulfide perovskites: reduction of the electronic band gap of $RbTaO_3$ by sulfur substitution, *Phys. Scr.*, 2024, **99**, 045950, DOI: 10.1088/1402-4896/ad31f3.

37 S. Tariq, O. Alsalmi, A. O. Alrashdi, A. A. Mubarak and B. Kanwal, Investigating the influence of pressure on $SrFeO_3$ and $SrMnO_3$ ferromagnets for high-pressure spintronic devices: a comparative DFT overview, *Appl. Phys. A*, 2021, **127**, 902, DOI: 10.1007/s00339-021-05052-0.

38 S. S. A. Gillani, R. Ahmad, M. Rizwan, M. Rafique, G. Ullah, C. B. Cao, *et al.*, Effect of magnesium doping on band gap and optical properties of $SrZrO_3$ perovskite: A first-principles study, *Optik*, 2019, **191**, 132–138, DOI: 10.1016/j.ijleo.2019.05.099.

39 A. Hosen, Investigating the effects of hydrostatic pressure on the physical properties of cubic Sr_3BCl_3 (B = As, Sb) for improved optoelectronic applications: A DFT study, *Heliyon*, 2024, **10**(16), e35855, DOI: 10.1016/j.heliyon.2024.e35855.

40 A. Hosen, M. R. Islam and J. Park, Pressure-Induced Band Gap Shifting from Ultra-violet to Visible Spectrum of Non-toxic $RbCaBr_3$ Cubic Perovskite for Enhancing Optoelectronic Applications, *J. Inorg. Organomet. Polym. Mater.*, 2024, **34**, 2378–2387, DOI: 10.1007/s10904-023-02970-9.

41 A. A. Mubarak and S. Tariq, Elucidating the effect of Pb and Ba substitution in $SrTcO_3$ for advanced radioactive semiconducting applications, *Opt. Quantum Electron.*, 2023, **55**, 614, DOI: 10.1007/s11082-023-04891-w.

42 N. H. Linh, N. H. Tuan, D. D. Dung, P. Q. Bao, B. T. Cong and L. T. H. Thanh, Alkali metal-substituted bismuth-based perovskite compounds: A DFT study, *J. Sci.:Adv. Mater. Devices*, 2019, **4**, 492–498, DOI: 10.1016/j.jsamd.2019.06.005.

43 Y. Shi, Z. Ma, D. Zhao, Y. Chen, Y. Cao, K. Wang, G. Xiao and B. Zou, Pressure-Induced Emission (PIE) of One-Dimensional Organic Tin Bromide Perovskites, *J. Am. Chem. Soc.*, 2019, **141**(16), 6504–6508, DOI: 10.1021/jacs.9b02568.

44 Z. Ma, Z. Liu, S. Lu, L. Wang, X. Feng, D. Yang, *et al.*, Pressure-induced emission of cesium lead halide perovskite nanocrystals, *Nat. Commun.*, 2018, **9**, 4506, DOI: 10.1038/s41467-018-06840-8.

45 Y. Fang, L. Zhang, L. Wu, J. Yan, Y. Lin, K. Wang, *et al.*, Pressure-Induced Emission (PIE) and Phase Transition of a Two-dimensional Halide Double Perovskite $(BA)_4AgBiBr_8$ ($BA=CH_3(CH2)_3NH^{3+}$), *Angew. Chem., Int. Ed.*, 2019, **58**, 15249–15253, DOI: 10.1002/anie.201906311.

46 Y. Wang, X. Lü, W. Yang, T. Wen, L. Yang, X. Ren, *et al.*, Pressure-Induced Phase Transformation, Reversible Amorphization, and Anomalous Visible Light Response in Organolead Bromide Perovskite, *J. Am. Chem. Soc.*, 2015, **137**, 11144–11149, DOI: 10.1021/jacs.5b06346.

47 M. Saeed, M. A. Ali, S. Murad, R. Ullah, T. Alshahrani, A. Laref, *et al.*, Pressure induced structural, electronic, optical and thermal properties of $CsYbBr_3$, a theoretical investigation, *J. Mater. Res. Technol.*, 2021, **10**, 687–696, DOI: 10.1016/j.jmrt.2020.12.052.

48 Q. Ou, X. Bao, Y. Zhang, H. Shao, G. Xing, X. Li, *et al.*, Band structure engineering in metal halide perovskite nanostructures for optoelectronic applications, *Nano Mater. Sci.*, 2019, **1**, 268–287, DOI: 10.1016/j.nanoms.2019.10.004.

49 Md. A. Rahman, R. Khatun, R. Ferdous, D. Chandra Roy, Md. Z. Hasan, A. Irfan, *et al.*, First-principles calculations to investigate structural, elastic, electronic, optical and thermal properties of La-based ternary intermetallic superconductors $LaM2Si_2$ (M=Co, Cu, Rh, Pd, Ag, Ir, Pt, Au), *J. Mater. Res. Technol.*, 2023, **26**, 3840–3862, DOI: 10.1016/j.jmrt.2023.08.177.

50 M. Atikur Rahman, M. Hasan, J. F. Lubna, R. Khatun, S. Sarker, M. Z. Hasan, *et al.*, Comparative study of the structural, mechanical, electronic, optical and thermodynamic properties of superconducting disilicide $YT2Si_2$ (T=Co, Ni, Ru, Rh, Pd, Ir) by DFT simulation, *J. Phys. Chem. Solids*, 2023, **178**, 111342, DOI: 10.1016/j.jpcs.2023.111342.

51 M. M. H. Babu, T. Saha, J. Podder, P. Roy, A. Barik and E. Haque, Electronic structure transition of cubic $CsSnCl_3$ under pressure: effect of rPBE and PBEsol functionals and GW method, *Heliyon*, 2021, **7**(8), e07796, DOI: 10.1016/j.heliyon.2021.e07796.

52 P. Giannozzi, O. Andreussi, T. Brumme, O. Bunau, M. B. Nardelli, M. Calandra, *et al.*, Advanced capabilities for materials modelling with Quantum ESPRESSO, *J. Phys.: Condens. Matter*, 2017, **29**, 465901, DOI: 10.1088/1361-648X/aa8f79.

53 P. Giannozzi, S. Baroni, N. Bonini, M. Calandra, R. Car, C. Cavazzoni, *et al.*, QUANTUM ESPRESSO: a modular and open-source software project for quantum simulations of materials, *J. Phys.: Condens. Matter*, 2009, **21**, 395502, DOI: 10.1088/0953-8984/21/39/395502.
54 J. Heyd, G. E. Scuseria and M. Ernzerhof, Hybrid functionals based on a screened Coulomb potential, *J. Chem. Phys.*, 2003, **118**, 8207–8215, DOI: 10.1063/1.1564060.
55 A. Togo and I. Tanaka, First principles phonon calculations in materials science, *Scr. Mater.*, 2015, **108**, 1–5, DOI: 10.1016/j.scriptamat.2015.07.021.
56 A. D. Corso, *Thermo Pw Driver v.1.7.0*, 2023, Welcome to Thermo_pw, https://dalcorso.github.io/thermo_pw/, accessed February 23, 2024.
57 O. H. Nielsen and R. M. Martin, First-Principles Calculation of Stress, *Phys. Rev. Lett.*, 1983, **50**, 697–700, DOI: 10.1103/PhysRevLett.50.697.
58 H.-J. Feng and Q. Zhang, Predicting efficiencies >25% A_3MX_3 photovoltaic materials and Cu ion implantation modification, *Appl. Phys. Lett.*, 2021, **118**, 111902, DOI: 10.1063/5.0039936.
59 M. A. Brogan, R. W. Hughes, R. I. Smith and D. H. Gregory, Structural studies of magnesium nitride fluorides by powder neutron diffraction, *J. Solid State Chem.*, 2012, **185**, 213–218, DOI: 10.1016/j.jssc.2011.11.008.
60 M. W. Qureshi, X. Ma, G. Tang and R. Paudel, Ab initio predictions of structure and physical properties of the Zr_2GaC and Hf_2GaC MAX phases under pressure, *Sci. Rep.*, 2021, **11**, 3260, DOI: 10.1038/s41598-021-82402-1.
61 W. Shangguan, C. Yan and J. Cai, Quasi-Planar tetracoordiante carbon Networks with tunable electronic properties combined with Ultra-High carrier mobility and optical absorption Coefficient: Two-dimensional Be_2C, *Appl. Surf. Sci.*, 2022, **604**, 154644, DOI: 10.1016/j.apsusc.2022.154644.
62 L. Liu, C. Yan, L. Gao, W. Shangguan, J. Dai and J. Cai, Structural stabilities, electronic structures, photocatalysis and optical properties of γ-GeN and α-SnP monolayers: a first-principles study, *Mater. Res. Express*, 2021, **8**, 125010, DOI: 10.1088/2053-1591/ac3fdc.
63 O. Reckeweg and F. J. DiSalvo, About Binary and Ternary Alkaline Earth Metal Nitrides, *Z. Anorg. Allg. Chem.*, 2001, **627**, 371–377, DOI: 10.1002/1521-3749(200103)627:3<371::AID-ZAAC371>3.0.CO;2-A.
64 A. Bach, D. Fischer, X. Mu, W. Sigle, P. A. van Aken and M. Jansen, Structural evolution of magnesium difluoride: from an amorphous deposit to a new polymorph, *Inorg. Chem.*, 2011, **50**, 1563–1569, DOI: 10.1021/ic1021615.
65 E. Zintl and E. Husemann, Bindungsart und Gitterbau binärer Magnesiumverbindungen, *Z. Phys. Chem.*, 1933, **21**, 138–155, DOI: 10.1515/zpch-1933-2112.
66 C. M. Widdifield and D. L. Bryce, Crystallographic structure refinement with quadrupolar nuclei: a combined solid-state NMR and GIPAW DFT example using $MgBr_2$, *Phys. Chem. Chem. Phys.*, 2009, **11**, 7120–7122, DOI: 10.1039/B911448N.
67 M. A. Brogan, A. J. Blake, C. Wilson and D. H. Gregory, Magnesium diiodide, MgI_2, *Acta Crystallogr., Sect. C:Cryst. Struct. Commun.*, 2003, **59**, i136–i138, DOI: 10.1107/S0108270103025769.
68 M. A. Brogan, R. W. Hughes, R. I. Smith and D. H. Gregory, Structural studies of magnesium nitride fluorides by powder neutron diffraction, *J. Solid State Chem.*, 2012, **185**, 213–218, DOI: 10.1016/j.jssc.2011.11.008.
69 S. Baroni, S. de Gironcoli, A. Dal Corso and P. Giannozzi, Phonons and related crystal properties from density-functional perturbation theory, *Rev. Mod. Phys.*, 2001, **73**, 515–562, DOI: 10.1103/RevModPhys.73.515.
70 A. Togo and I. Tanaka, First principles phonon calculations in materials science, *Scr. Mater.*, 2015, **108**, 1–5, DOI: 10.1016/j.scriptamat.2015.07.021.
71 N. T. Mahmoud, A. A. Mousa and J. M. Khalifeh, First principles investigation of thermoelectric and mechanical properties of $VScO_3$ semiconductor perovskite for sustainable and renewable energy, *Results Phys.*, 2020, **18**, 103331, DOI: 10.1016/j.rinp.2020.103331.
72 H. Liu, J. Yang, Y. Jia, Z. Wang, M. Jiang, K. Shen, *et al.*, Significant Improvement of Catalytic Performance for Chlorinated Volatile Organic Compound Oxidation over RuOx Supported on Acid-Etched Co_3O_4, *Environ. Sci. Technol.*, 2021, **55**, 10734–10743, DOI: 10.1021/acs.est.1c02970.
73 J. Liu, Y. Yin, K. Wang, P. Wei, H. Lu, C. Song, *et al.*, Domain size control in all-polymer solar cells, *iScience*, 2022, **25**, 104090, DOI: 10.1016/j.isci.2022.104090.
74 C. M. Zener and S. Siegel, *Elasticity and Anelasticity of Metals*, ACS Publications, 2002, DOI: 10.1021/j150474a017.
75 W. Azeem, S. Hussain, M. K. Shahzad, F. Azad, G. Khan, V. Tirth, *et al.*, Computational insights of double perovskite X_2CaCdH_6 (X = Rb and Cs) hydride materials for hydrogen storage applications: A DFT analysis, *Int. J. Hydrogen Energy*, 2024, **79**, 514–524, DOI: 10.1016/j.ijhydene.2024.07.044.
76 M. Caid, D. Rached, Y. Rached and H. Rached, Comprehensive exploration of halide double perovskites $Cs_2B'GeCl_6$ (B′: Zn, Cd) for affordable energy technologies: a high-throughput investigation, *Opt. Quantum Electron.*, 2024, **56**, 980, DOI: 10.1007/s11082-024-06721-z.
77 S. Hussain and J. U. Rehman, First-principles calculation to investigate structural, electronic, optical, and thermodynamics properties of perovskite KXO_3 (KTa and Zn) alloys for photovoltaic and smart window applications, *Phys. B*, 2024, **687**, 416116, DOI: 10.1016/j.physb.2024.416116.
78 D. Music, Z. Sun, R. Ahuja and J. M. Schneider, Electronic structure of $M_2AlC(0001)$ surfaces (M = Ti,V,Cr), *J. Phys.: Condens. Matter*, 2006, **18**, 8877, DOI: 10.1088/0953-8984/18/39/017.
79 N. Miao, B. Sa, J. Zhou and Z. Sun, Theoretical investigation on the transition-metal borides with Ta3B4-type structure: A class of hard and refractory materials, *Comput. Mater. Sci.*, 2011, **50**, 1559–1566, DOI: 10.1016/j.commatsci.2010.12.015.
80 X.-Q. Chen, H. Niu, D. Li and Y. Li, Modeling hardness of polycrystalline materials and bulk metallic glasses,

Intermetallics, 2011, **19**, 1275–1281, DOI: 10.1016/j.intermet.2011.03.026.

81 C. Jasiukiewicz and V. Karpus, Debye temperature of cubic crystals, *Solid State Commun.*, 2003, **128**, 167–169, DOI: 10.1016/j.ssc.2003.08.008.

82 O. L. Anderson, A simplified method for calculating the debye temperature from elastic constants, *J. Phys. Chem. Solids*, 1963, **24**, 909–917, DOI: 10.1016/0022-3697(63)90067-2.

83 E. Schreiber, O. L. Anderson, N. Soga and J. F. Bell, Elastic Constants and Their Measurement, *J. Appl. Mech.*, 1975, **42**, 747–748, DOI: 10.1115/1.3423687.

84 P. Deus and H. A. Schneider, Estimation of the debye temperature of diamond-like semiconducting compounds from bulk modul and microhardness, *Cryst. Res. Technol.*, 1983, **18**, 491–500, DOI: 10.1002/crat.2170180410.

85 Y. Zhang, First-principles Debye–Callaway approach to lattice thermal conductivity, *Journal of Materiomics*, 2016, **2**, 237–247, DOI: 10.1016/j.jmat.2016.06.004.

86 M. Khalid Hossain, A. A. Arnab, R. C. Das, K. M. Hossain, M. H. K. Rubel, M. Ferdous Rahman, *et al.*, Combined DFT, SCAPS-1D, and wxAMPS frameworks for design optimization of efficient $CsBiAgI_6$-based perovskite solar cells with different charge transport layers, *RSC Adv.*, 2022, **12**, 35002–35025, DOI: 10.1039/D2RA06734J.

87 K.-E. Peiponen, V. Lucarini, E. M. Vartiainen and J. J. Saarinen, Kramers-Kronig relations and sum rules of negative refractive index media, *Eur. Phys. J. B*, 2004, **41**, 61–65, DOI: 10.1140/epjb/e2004-00294-6.

88 A. Hossain, M. A. Ali, M. M. Uddin, S. H. Naqib and M. M. Hossain, Theoretical studies on phase stability, electronic, optical, mechanical and thermal properties of chalcopyrite semiconductors $HgXN_2$ (X=Si, Ge and Sn): A comprehensive DFT analysis, *Mater. Sci. Semicond. Process.*, 2024, **172**, 108092, DOI: 10.1016/j.mssp.2023.108092.

89 T. Baikie, N. S. Barrow, Y. Fang, P. J. Keenan, P. R. Slater, R. O. Piltz, *et al.*, A combined single crystal neutron/X-ray diffraction and solid-state nuclear magnetic resonance study of the hybrid perovskites $CH3NH_3PbX_3$ (X = I, Br and Cl), *J. Mater. Chem. A*, 2015, **3**, 9298–9307, DOI: 10.1039/C5TA01125F.

90 E. Mosconi, P. Umari and F. D. Angelis, Electronic and optical properties of $MAPbX_3$ perovskites (X = I, Br, Cl): a unified DFT and GW theoretical analysis, *Phys. Chem. Chem. Phys.*, 2016, **18**, 27158–27164, DOI: 10.1039/C6CP03969C.

91 T. Yang, C. Yan, S. Qiu, Y. Tang, A. Du and J. Cai, First-Principles Study of Penta-PtXY (X = Se, Te; Y = S, Te; X ≠ Y) Monolayer with Highly Anisotropic Electronic and Optical Properties, *ACS Omega*, 2024, **9**, 32502–32512, DOI: 10.1021/acsomega.4c00803.

92 W. Shangguan, C. Yan, W. Li, C. Long, L. Liu, C. Qi, *et al.*, Two-dimensional semiconductor materials with high stability and electron mobility in group-11 chalcogenide compounds: MNX (M = Cu, Ag, Au; N = Cu, Ag, Au; X = S, Se, Te; M ≠ N), *Nanoscale*, 2022, **14**, 4271–4280, DOI: 10.1039/D1NR06971C.

93 C. Qi, C. Yan, Q. Li, T. Yang, S. Qiu and J. Cai, Two-dimensional Janus chalcogenides: candidates for efficient photocatalysts and piezoelectric materials, *J. Mater. Chem. A*, 2024, **12**, 3542–3556, DOI: 10.1039/D3TA06340B.

94 M. E. Fine, L. D. Brown and H. L. Marcus, Elastic constants versus melting temperature in metals, *Scr. Metall.*, 1984, **18**, 951–956, DOI: 10.1016/0036-9748(84)90267-9.

95 D. R. Clarke, Materials selection guidelines for low thermal conductivity thermal barrier coatings, *Surf. Coat. Technol.*, 2003, **163–164**, 67–74, DOI: 10.1016/S0257-8972(02)00593-5.

96 G. A. Slack, The Thermal Conductivity of Nonmetallic Crystals, in *Solid State Physics*, ed. Ehrenreich H., Seitz F. and Turnbull D., Academic Press, 1979, vol. 34, pp. 1–71, DOI: 10.1016/S0081-1947(08)60359-8.

97 M. Sarwan, V. A. Shukoor, M. F. Shareef and S. Singh, A first principle study of structural, elastic, electronic and thermodynamic properties of Half-Heusler compounds; YNiPn (Pn=As, sb, and bi), *Solid State Sci.*, 2021, **112**, 106507, DOI: 10.1016/j.solidstatesciences.2020.106507.

98 H. Akter, M. M. Hossain, M. M. Uddin, S. H. Naqib and M. A. Ali, Effects of S substitution on the structural, optoelectronic, and thermomechanical properties of $KTaO_3$ through density functional theory, *J. Phys. Chem. Solids*, 2024, **190**, 112021, DOI: 10.1016/j.jpcs.2024.112021.

99 R. Islam, M. M. Hossain, M. A. Ali, M. M. Uddin and S. H. Naqib, Metallic boro-carbides of A_2BC (A = Ti, Zr, Hf and W): a comprehensive theoretical study for thermo-mechanical and optoelectronic applications, *RSC Adv.*, 2022, **12**, 32994–33007, DOI: 10.1039/D2RA05448E.

100 P. Debye, Zur Theorie der spezifischen Wärmen, *Ann. Phys.*, 1912, **344**, 789–839, DOI: 10.1002/andp.19123441404.

101 R. Fox, The Background to the Discovery of Dulong and Petit's Law, *Br. J. Hist. Sci.*, 1968, **4**, 1–22, DOI: 10.1017/S0007087400003150.